Feasibility Study for a High-Frequency Flexible Ultrasonic Cuff for High-Precision Vagus Nerve Ultrasound Neuromodulation

Van Damme, Cornelis; Wardhana, Gandhika K.; Velea, Andrada Iulia; Giagka, Vasiliki; Costa, Tiago L.

DOI
10.1109/TUFFC.2024.3381923

Publication date
2024

Document Version
Final published version

Published in
IEEE Transactions on Ultrasonics, Ferroelectrics, and Frequency Control

Feasibility Study for a High-Frequency Flexible Ultrasonic Cuff for High-Precision Vagus Nerve Ultrasound Neuromodulation

Cornelis van Damme, Gandhika K. Wardhana, *Graduate Student Member, IEEE*, Andrada Iulia Velea, *Graduate Student Member, IEEE*, Vasiliki Giagka, *Senior Member, IEEE*, and Tiago L. Costa, *Senior Member, IEEE*

***Abstract*—In the emerging research field of bioelectronic medicine, it has been indicated that neuromodulation of the vagus nerve (VN) has the potential to treat various conditions such as epilepsy, depression, and autoimmune diseases. In order to reduce side effects, as well as to increase the effectiveness of the delivered therapy, sub-fascicle stimulation specificity is required. In the electrical domain, increasing spatial selectivity can only be achieved using invasive and potentially damaging approaches like compressive forces or nerve penetration. To avoid these invasive methods while obtaining a high spatial selectivity, a 2-mm diameter extraneural cuff-shaped proof-of-concept design with integrated lead zirconate titanate (PZT) based ultrasound (US) transducers is proposed in this article. For the development of the proposed concept, wafer-level microfabrication techniques are employed. Moreover, acoustic measurements are performed on the device, in order to characterize the ultrasonic beam profiles of the integrated PZT-based US transducers. A focal spot size of around 200 × 200 μm is measured for the proposed cuff. Moreover, the curvature of the device leads to constructive interference of the US waves originating from multiple PZT-based US transducers, which in turn leads to an increase of 45% in focal pressure compared to the focal pressure of a single PZT-based US transducer. Integrating PZT-based US transducers in an extraneural cuff-shaped design has the potential to achieve high-precision US neuromodulation of the VN without requiring intraneural implantation.**

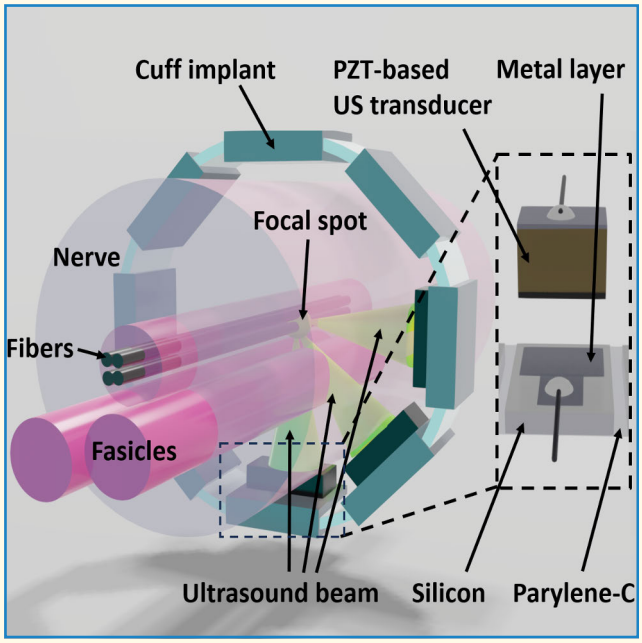

***Index Terms*— Cuff implant, flex-to-rigid, lead zirconate titanate (PZT) integration, microfabrication, piezoelectric ultrasound (US) transducers, US neuromodulation, vagus nerve (VN).**

I. Introduction

THE application of ultrasound (US) technologies in the medical field has been extended from diagnostic imaging to therapeutic neuromodulation [1], [2], [3]. Among several stimulation targets, vagus nerve stimulation (VNS) by means of focused US has been explored in recent years [4], [5], [6], [7]. The vagus nerve (VN) is a cranial nerve, part of the parasympathetic nervous system, consisting of afferent and efferent neurons [8], [9], [10], [11]. At the level of the neck, the VN is more easily accessible. The VN comprises fascicles in which about a hundred thousand fibers are bundled together. The different nerve fibers, classified, according to Erlanger Gasser, as type A, B, and C, each have their own functions, sizes (ranging from <0.5 up to 10 μm), and conduction velocities (ranging from 0.5 to 120 m/s) [8], [9]. The VN is involved in the autonomic, cardiovascular, respiratory, gastrointestinal, immune, and endocrine systems [8]. Research shows that stimulation is useful in the therapy of epilepsy, depression, and several chronic diseases like Alzheimer's disease, anxiety, congestive heart failure, pain, tinnitus, and inflammatory diseases [8], [11], [12], [13], [14], [15], [16].

Manuscript received 30 January 2024; accepted 21 March 2024. Date of publication 26 March 2024; date of current version 15 July 2024. This work was supported in part by the Electronic Components and Systems for European Leadership (ECSEL) Joint Undertaking project Moore4Medical under Grant H2020-ECSEL-2019IA-876190 and in part by CHIPS Joint Undertaking NerveRepack, under Grant nº 101112347. *(Vasiliki Giagka and Tiago L. Costa contributed equally to this work.) (Corresponding author: Cornelis van Damme.)*

Cornelis van Damme, Gandhika K. Wardhana, and Tiago L. Costa are with the Department of Microelectronics, Delft University of Technology, 2628 CD Delft, The Netherlands (e-mail: nvdamme@hotmail.nl; t.m.l.dacosta@tudelft.nl).

Andrada Iulia Velea and Vasiliki Giagka are with the Department of Microelectronics, Delft University of Technology, 2628 CD Delft, The Netherlands, and also with the Department of System Integration and Interconnection Technologies, Fraunhofer IZM, 13355 Berlin, Germany (e-mail: v.giagka@tudelft.nl).

Digital Object Identifier 10.1109/TUFFC.2024.3381923

Highlights

- **Integration of PZT-based US transducers in a wafer-level microfabricated cuff-implant for VN US neuromodulation.**
- **A 2-mm diameter curved, wafer-level microfabricated cuff-implant with embedded PZT-based US transducers shows constructive interference at the focal spot, thus increasing the output focal pressure.**
- **A novel, highly specific, high-frequency, extraneural cuff-implant that enables sub-fascicle level VN US neuromodulation.**

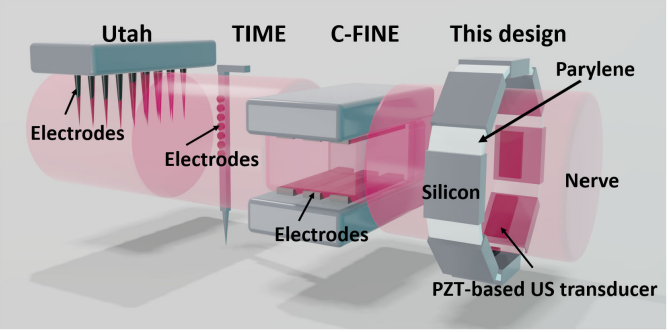

Fig. 1. Comparison of the Utah, TIME, and C-FINE electrodes with the current design.

Targeted stimulation on the sub-fascicle level is needed since unintended stimulation of other fascicles can lead to severe side effects like pain, dyspnea, or temporary facial paresis [16], [17], [18].

Conventionally, electricity is used to interact with the peripheral nervous system [19]. Transcutaneous VNS (tVNS) has been proposed as a noninvasive method [16], [20], [21], [22], [23], [24]. Although studies show that activation is elicited, the envisioned sub-fascicle stimulation resolution is not met [25]. Improved resolution can be achieved with implantable devices having embedded electrodes. A promising type of electrode for stimulation is the cuff electrode [26], [27], [28], [29], [30]. To reach the sub-fascicle resolution with electrodes, techniques like composite flat interface nerve electrodes (C-FINE) [31], slowly penetrating interfascicular nerve electrodes (SPINE) [32] and intrafascicular techniques like longitudinal intrafascicular electrode (LIFE) [26] and transverse intrafascicular multichannel electrode (TIME) [26] and microelectrode arrays (MEAs), for example, the Utah array [33], are being developed [34]. The disadvantages of the aforementioned techniques are the needed compressive force and high invasiveness, which increase the risk of damage to the nerve during implantation (see Fig. 1). Therefore, this makes these techniques unsuitable for chronic applications.

Instead of using electrodes, integrating lead zirconate titanate (PZT) based US transducers in a cuff implant form factor would enable the possibility of delivering US neuromodulation extraneurally, yet with a high spatial resolution (see Fig. 1). It has been previously demonstrated that a focal spot of 110 × 570 μm can be achieved when capacitive micromachined ultrasound transducers (CMUTs) are placed under the nerve and are geometrically curved at radii matching that of the VN [7]. Based on the well-described physical phenomena of US, it has been shown that US can be beam steered [35], [36] and can propagate through tissue for several centimeters without causing damage and side effects [2], [3], [37], [38]. Depending on the parameters of the US exposure, tissue damage, and severe thermal effects can occur [4], [39], [40]. This is used for high-intensity focused ultrasound (HIFU) to ablate tissue [41]. However, this is not intended in this research as the signal parameters are substantially different.

Despite the biological mechanisms of US neuromodulation not yet being perfectly understood, it is likely that different combinations of partially overlapping mechanisms occur in the cell membrane depending on the US pulse regime [2], [3], [4], [40], [42], [43], [44]. Several studies show that focused US can elicit a physiological response in nerves, including the VN [4], [5], [6], [29], [39], [40], [45], [46], [47]. In addition, new techniques for marking neuronal activation, such as Fos proto-oncogene (c-FOS), have been used to verify the efficacy of focused US VNS in eliciting activity in the brain [48].

US waves are generated by either bulk piezoelectric transducers or by flexural mode transducers, such as CMUTs and piezoelectric micromachined ultrasound transducers (PMUTs) [35], [49], [50], [51], [52]. For bulk mode PZT-based US transducers, which are characterized by a high transmit electroacoustic sensitivity ($S_{tx} = (P_{peak}/V_{driving})$, where P_{peak} is the peak output pressure [kPa] and $V_{driving}$ the driving voltage [V]) and a high-quality factor [35], PZT ceramics are commonly used due to their superior piezoelectric constants [55]. These are important characteristics for US neuromodulation as they lead to higher and more stable pressure amplitudes per driving voltage [35], [49], [50]. In general, PMUT and CMUT devices have a lower S_{tx} [53], [54] and lower quality factor, and hence are more suitable for high-quality imaging and sensing applications where bandwidth is important [35], [55]. Optimization techniques, such as using substrate-embedded springs [56] or operating in collapse mode [57], can achieve S_{tx} similar to that of bulk PZT. Moreover, PMUT and CMUT devices exhibit lower mechanical impedance, making them inherently better acoustically matched to biological tissue. However, transduction in flexural mode transducers involves applying an ac signal across a suspended flexural membrane. This imposes a maximum safe driving voltage limit before device breakdown and constrains the maximum generated acoustic pressure with safe in vitro and/or in vivo voltage levels. The pressure output of an integrated CMUT-array in a cuff implant form factor using 25 V_{pp} for excitation with beam steering has been measured to generate 1.7 MPa at most (S_{tx} = 68 kPa/V) [36]. Another planar design with a 2-D PZT-based

TABLE I
DESIGN PARAMETERS

Parameters	Numbers
Driving frequency $[MHz]$	8.4
Diameter $[mm]$	2
# of PZT-based US transducers	3
PZT thickness $[\mu m]$	254
PZT aperture $[\mu m]$	1100
PZT length $[\mu m]$	450
Focal length $[mm]$	1
Active area $[mm^2]$	1.49

US transducer array with 5 V_{pp} generated up to 0.1 MPa ($S_{tx} = 20$ kPa/V) [35]. As the output pressure correlates with the driving voltage [58] and the focusing of the beam, S_{tx} is a good parameter for comparison.

Currently, there is no consensus on the intensity or pressure needed for neuromodulation of peripheral nerves. However, research suggests that peripheral nerves require higher pressures than, e.g., brain tissue for neuromodulation and that pressures in the range of 3 MPa are sufficient [4]. To date, a method to integrate bulk PZT-based US transducers in a miniaturized, flexible cuff compatible with VNS has not yet been demonstrated [25].

In this article, a first prototype of a form factor compatible with the VN with integrated PZT-based US transducers is proposed. Unlike previous research, this design is developed for neuromodulation of a nerve, requiring a miniaturized and curvable design. We investigate whether this design can reach high acoustic pressures with low peak-to-peak driving voltages and still maintain high spatial resolution. The organization of this article is as follows: in Section II the design choices and the necessary COMSOL Multiphysics [59] simulations are elaborated upon. Section III describes the design and elaborates on the wafer-level microfabrication process flow and the assembly of the PZT-based cuff prototypes (see Section III-A). In Section IV the device is characterized and the acoustic measurements are described. The results are discussed in Section V, whereas Section VI draws the conclusions.

II. SIMULATIONS

The concept, shown in Fig. 1, is a cuff-shaped, island-bridge structure with three 8.4-MHz PZT-based US transducers. In Table I the main design parameters are given. The inner diameter of the cuff is 2 mm, as the VN has a diameter of about 2–4 mm [7]. The aperture of the PZT relates to the focal length and driving frequency according to [60]

$$N = \frac{f_p L^2}{4v} \tag{1}$$

where N is the focal length [m], L the aperture [m], f_p the driving frequency [Hz] and v the speed of sound in the medium [m/s]. The focal point of all PZT-based US transducers comprising the cuff has been designed to be around 1 mm, such that it is in the center of the design, as well as, of the nerve. PZT material is not flexible, and embedding large PZT transducers in the cuff design would limit the flexibility and the ability to be circular shaped. Avoiding the PZTs limiting the circular shape of the cuff, the aperture of single PZTs is not larger than the chord of 12.5% of the circumference.

Frequencies for neuromodulation in preclinical or clinical research can scale from sub-MHz (transcranial US neuromodulation) to a few MHz (VNS). Increasing the driving frequency leads to a tradeoff between spatial resolution and absorption. Hence, the driving frequency should be carefully set. The driving frequency is inversely proportional to the aperture (1), the focal spot size (2) and (3), and the thickness (4) of the PZT [49], [60]. The equations for the full width at half bandwidth FHWM [35], the depth of field DOF [35], and thickness of the PZT at resonance (t_{PZT}) [55] are given in the following equations, respectively,

$$\text{FWHM} \propto \frac{\lambda Z_m}{L} \tag{2}$$

where λ is the wavelength of the US waves [m], Z_m is the focal depth [m] and L the aperture [m]

$$\text{DOF} \propto \frac{\lambda Z_m^2}{L^2} \tag{3}$$

$$t_{PZT} = \frac{\lambda}{2}. \tag{4}$$

In this study, it has been assumed that the acoustic wave is propagating in a homogeneous medium and that there is no gap between the implant and the nerve. Moreover, since the interelement space between the PZTs is limited and neighboring PZTs should not touch each other in the circular cuff, the PZT thickness should be in the range of the silicon thickness (around 300 μm). This is a direct constraint for the driving frequency (4). Furthermore, this driving frequency determines the aperture, whereas the aperture is a tradeoff between the focal length and the maximum PZT size allowed within the circular shape. Therefore, the driving frequency should be as high as possible to have a high spatial resolution, yet the PZT-based US transducer size fits the design dimensions and obeys the restrictions for the circular shape. Therefore, a driving frequency of 8.4 MHz has been set. Moreover, other research shows that similar driving frequencies (9.56 and 8.4 MHz) provide resolution in the μm-range [35], [60] and PZT-transducers having this driving frequency are commercially available.

A. Methods

To define the effect of the number of PZT-based US transducers and to verify the design, COMSOL Multiphysics simulations have been performed. The 2-D finite element method simulations have been conducted in the frequency domain, using the pressure acoustics, solid mechanics, and electrostatics COMSOL models. A free triangular mesh with a maximum element size of $v/f_p/8$ has been used. Water medium has been used as a replacement for nerve tissue since the acoustic properties are similar [49]. The boundary of the water medium is set to be perfectly matched to avoid reflections at the edges. In addition, PZT-5H has been used

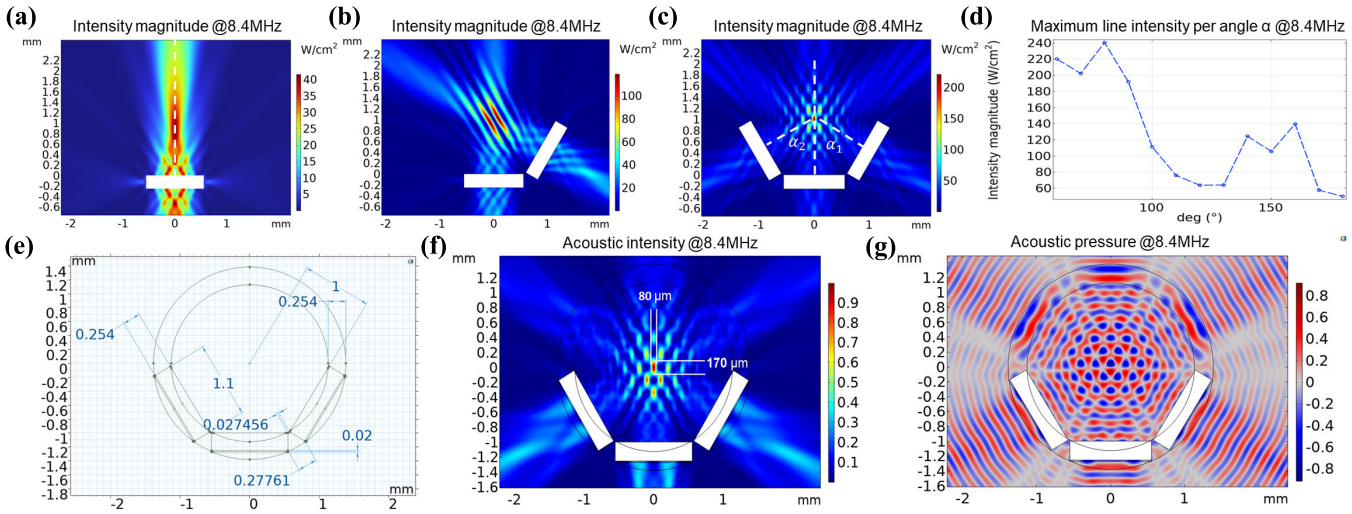

Fig. 2. Simulation results (a)–(c) show the focal spot size and acoustic intensity for one, two, and three PZT-based US transducers in a curved configuration. (d) Relation between the angle between three PZT-based US transducers and the maximum acoustic intensity magnitude. (e) Dimensions for the simulated cuff design, whereas (f) and (g) show the acoustic intensity magnitude and pressure profiles, respectively.

as a piezoelectric material for the PZT-based US transducers and a driving voltage of 10 V_{pp} has been defined, being the maximum output voltage of the function generator used during measurements (see Section IV). To ensure the focal point is in the center of the device, the distance between the surface of a PZT-based US transducer and the center has been set to 1 mm.

The first simulation has been done to investigate the effect of the number of PZT-based US transducers on the acoustic profile and pressure levels. The number of PZT-based US transducers has been swept from an individual PZT-based US transducer to three PZT-based US transducers. The next simulation is a rotational sweep of the angles α_1, α_2 which are the angles between one of the side PZT-based US transducers and the bottom-middle PZT-based US transducer [see Fig. 2(c)]. These angles are equal for the left and right side ($\alpha_1 = \alpha_2$) and are being swept from 50° to 180°.

Later, a full design with three PZT-based US transducers and a polymer ring of parylene-C was simulated to verify the focal spot and the design dimensions. The cuff implant form factor has been modeled as a perfect circle. The simulation dimensions are shown in Fig. 2(e).

B. Results

From simulations, it was found that the increase in the number of PZT-based US transducers increases the acoustic intensity magnitude in case they are placed in a curved configuration. According to the simulations, the focal intensity is 40 W/cm^2 for one PZT-based US transducer and increases to 120 W/cm^2 for two PZT-based US transducers and to 210 W/cm^2 for three PZT-based US transducers [see Fig. 2(a)–(c)], respectively. The increase of the acoustic intensity becomes less significant as more PZT-based US transducers are added. Moreover, with more PZT-based US transducers the focal spot size decreases, and destructive interference patterns appear.

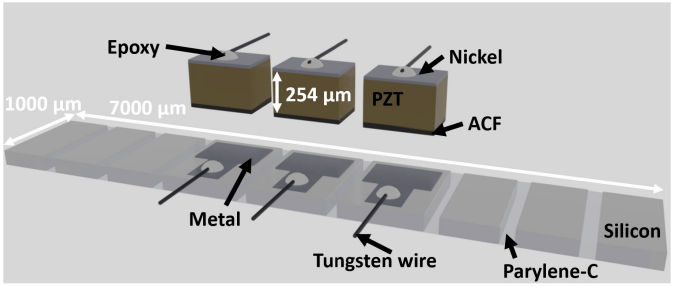

Fig. 3. Planar design of the proposed cuff implant.

The result of a sweep of three PZT-based US transducers is shown in Fig. 2(d). It can be observed that for smaller angles between the PZT-based US transducers, a higher acoustic intensity magnitude exists in this form factor. The intensity for an angle of 180°, so the PZT-based US transducers oppose each other, is reduced to 75% of the maximum acoustic intensity magnitude. Although opposite-placed PZT-based US transducers might be beneficial in different designs and in cases of beam steering, in this design, it has been concluded, based on this simulation, that opposite-placed PZT-based US transducers should be avoided. This limits the placement of PZT-based US transducers to only 40% of the cuff circumference.

Moreover, the number of PZT-based US transducers is determined by the aperture of the PZTs and the inter-PZT distance. The aperture of the PZTs is set by the aforementioned driving frequency. The inter-PZT distance between the PZT-based US transducers when curved, is optimized to be a multiple of $\lambda_{water}/2$ for minimizing the sidelobes while having the smallest distance [see Fig. 2(d)]. For a driving frequency of 8.4 MHz, three PZT-based US transducers do fit in the 2-mm cuff design [see Fig. 2(e)].

The acoustic intensity magnitude and pressure profiles for the cuff implant design can be found in Fig. 2(f) and (g), respectively. The acoustic waves are emitted from both the front- and back-side of the PZT-based US transducer. Note

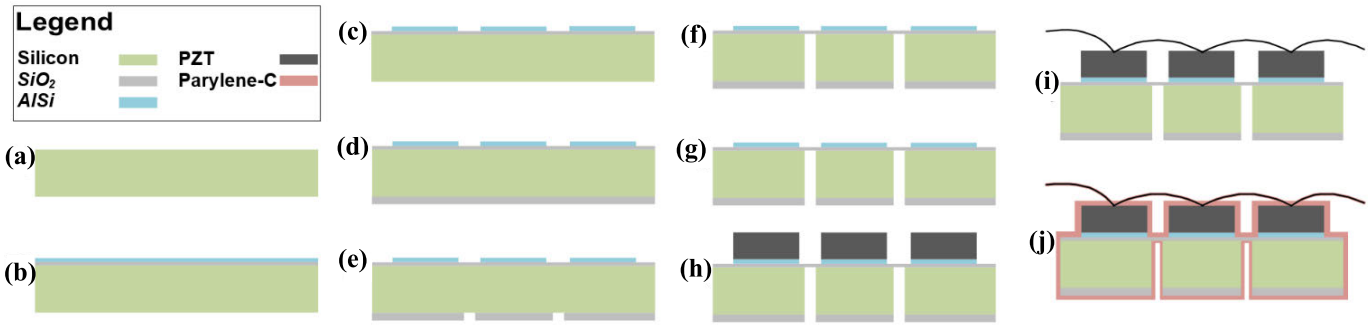

Fig. 4. Wafer-level microfabrication process steps. (a) Process starts with a wafer on which alignment markers are etched. (b) Layer of SiO_2 and on top a layer of AlSi is deposited. (c) AlSi layer is patterned. (d) SiO_2 layer is deposited at the backside. (e) SiO_2 at the backside is patterned. (f) Silicon substrate is etched from the backside. (g) Wafer is diced. (h) PZTs are placed on top. (i) Tungsten wire is attached on top of the PZTs. (j) Device is encapsulated with parylene-C.

that in COMSOL the intensity is a vector, whereas the pressure is a scalar, resulting in different profiles. It can be observed that the focal spot for the acoustic intensity has a size of 80 $\times$ 170 μm, and it is located in the center of the cuff shape.

III. Design

The development of the proposed cuff is based on wafer-level microfabrication processes [35], [61], [62], [63]. For this purpose, silicon has been selected as a substrate as it is a common substrate material within microfabrication. As a piezoelectric material, PZT-5H has been chosen as it is relatively cheap and robust compared to single-crystal piezoelectrics. In addition, it has a higher coupling coefficient than, for example, PZT-5A. The flexibility of the final device is provided by the island-bridge approach. Silicon islands are etched and after interconnected with each other via a parylene-C layer supported by a SiO_2 membrane (see Fig. 3). Parylene-C is known due to its high water vapor barrier, high chemical inertness, high heat resistance, and thin, conformal coating properties during chemical vapor deposition [64], [65]. In addition, it is mechanically flexible and therefore used as the flexible interconnect between the silicon islands in the island-bridge design. The metal layer provides the electrical connection to the PZT-based US transducers (see Fig. 3). The contact pads (500 $\times$ 500 μm) are directly connected to this metal layer with 500-μm-width traces.

The single planar device is 7 $\times$ 1 mm (see Fig. 3). According to the simulations in Section II, the resonance frequency and, thus, the driving frequency of the cuff concept is 8.4 MHz, resulting in a PZT thickness of around 254 μm. Taking the design constraints into account, only three PZT-based US transducers can be placed (see Fig. 3). The sizes of the PZT-based US transducers can be found in Table I.

A. Wafer-Level Microfabrication

The processing steps for the proposed wafer-level microfabrication process can be found in Fig. 4. A 300-μm-thick double-sided polished 100-mm diameter silicon wafer has been used as a starting material [see Fig. 4(a)]. On top of the wafer 1 μm of plasma-enhanced chemical vapor deposition (PECVD) oxide is deposited at 400 °C for insulation and as

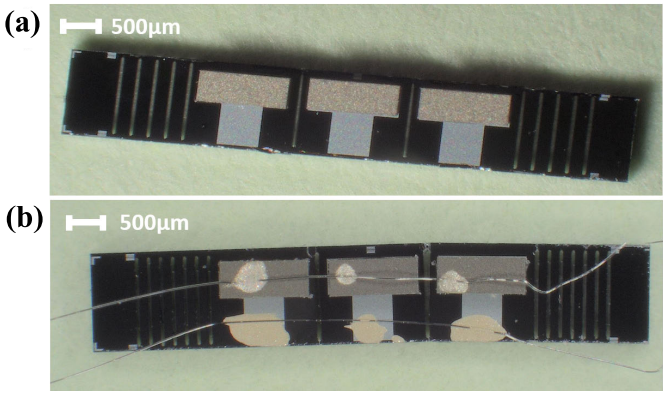

Fig. 5. Design and fabricated device. (a) Microscopic topview of a single, microfabricated device after step h. (b) Micrograph of the fabricated device after the attachment of tungsten wire (step i).

a landing layer for deep reactive ion etching (DRIE) from the backside of the wafer, required later in the process. On top of this layer, a metal interconnect layer of 1-μm-thick AlSi (99%/1%) is sputtered at 50 °C [see Fig. 4(b)]. AlSi (99%/1%) has been used due to its high conductivity, low cost, and availability. This metal layer is patterned using a 2.1-μm-thick positive photoresist (SPR3012, Shipley) as a soft mask and is etched using HBr/Cl_2-based dry etching processes [see Fig. 4(c)].

Next, a 4-μm-thick PECVD SiO_2 layer at 400° is deposited at the backside as a hard mask [see Fig. 4(d)]. The PECVD oxide layer at the backside is opened using a fully dry etch step [see Fig. 4(e)]. For this etch step a 3.1-μm-thick positive photoresist (SPR3012, Shipley) as soft mask has been used. Afterward, the bulk silicon of the wafer is etched till the SiO_2 layer at the top side using DRIE [see Fig. 4(f)]. This creates a 1-μm-thick SiO_2 membrane in between rigid, silicon islands. This SiO_2 membrane serves as support during the parylene-C coating later on in the process.

Next, the wafer is diced in a two-phase dicing process [see Fig. 4(g)] using the dicer (DAD3221, Disco). In the first phase, the wafer is attached with the top side to an ultraviolet-sensitive dicing foil and the wafer is diced into several larger pieces of around 3 $\times$ 3 mm^2. After releasing, each piece is individually diced into separate devices. For this phase, an acetone-sensitive dicing foil is used since the

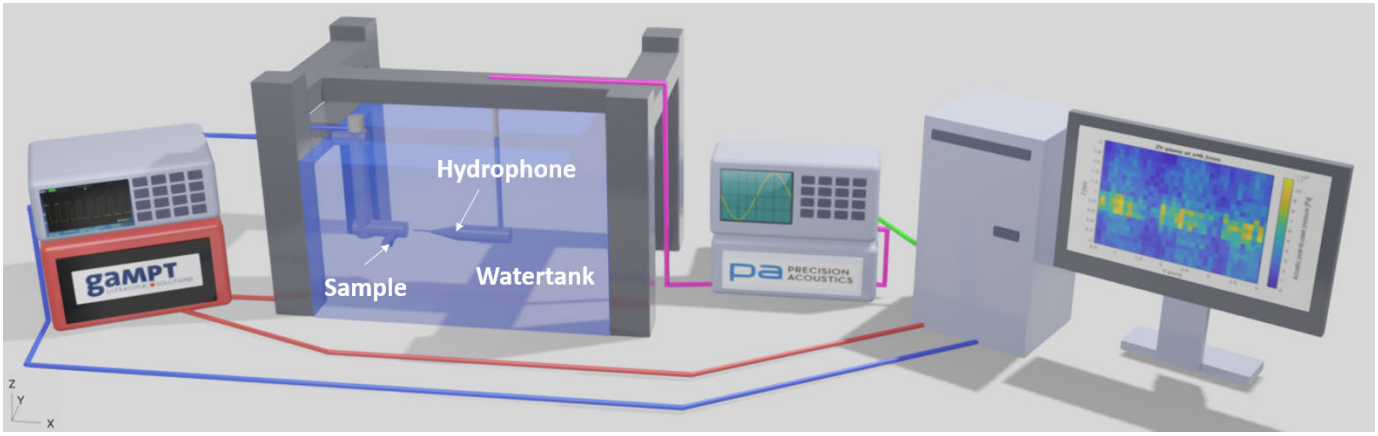

Fig. 6. Measurement setup from left to right: the function generator, the 3-D-axis motorized stage, the watertank with a hydrophone, the oscilloscope, the hydrophone amplifier, and the computer with software.

devices can be self-released from the foil using acetone, thus preserving the thin SiO_2 membrane. To maintain the thin SiO_2 membrane during dicing, the dicing speed is set to 1 mm/s, and a thin silicon edge (10 μm) is preserved, which does not interfere during the bending process. Commercial PZT-5H with a thickness of 267 μm from piezo.com are used for the PZT-based transducer. The chosen thickness is close to the simulated value, which should result in a similar mechanical resonance frequency. For conduction purposes, a 30-μm-thick anisotropic conductive film (ACF, ARclad 9032-70) is attached to one side of the PZT-5H sheet before dicing. The other side of the PZT has a 0.1-μm sputtered nickel layer (see Fig. 3). The PZT-sheet with ACF is diced into the sizes presented in Table I. With the pick-and-place tool (T-300 bonder, Accelonix), the PZTs are precisely (a tolerance of 10 μm) placed on the metal contact rings at the silicon substrate [see Fig. 4(h)]. Despite the beam splitter being used for alignment, some spatial variation exists.

The top connection between the PZT-based US transducers is made with 50-μm-thick tungsten wire which is connected using a layer of silver conductive paste (42469, Thermofischer). After curing, a layer of conductive epoxy (EPOTEK-H20E, Epoxy technology) is applied. This gives a mechanically robust and electrically conductive connection. To avoid, mechanical interference of the wires during the curvature of the device, each PZT and contact pad is individually connected with a tungsten wire [see Fig. 4(i)]. Afterward, the wires of the three contact pads are bundled as the wires of the three PZT-based US transducers. In this way, two connections, one for the ground and one for the signal, are available during the measurements. After the attachment of the tungsten wire, the device is encapsulated [see Fig. 4(j)] using a 5-μm-thick parylene-C coating (PDS 2010, Specialty coating systems). A micrograph of a single device after step h [see Fig. 4(h)] is shown in Fig. 5(a). Fig. 5(b) shows a micrograph of a device with attached wires.

IV. Characterization

The characterization has been done to show the impact of curvature on the focal spot. For the measurements, a device has been measured in a planar and curved configuration. The measurements are done in a water tank in which the device is fixed in a 3-D-printed holder to guarantee a precisely controlled and fixed curvature. The measurement setup is shown in Fig. 6. A function generator (DG4202, RIGOL) drives the device, generating a 10 V_{pp}, 30 pulses, 8.3 MHz, 1-ms period burst. The US pressure is measured using a fiber-optic hydrophone (FSV2-5580-10, Precision Acoustics) which is put into position with a 3-D-axis motorized stage (SFS630, GAMPT soundfield scanning drive). The fiber-optic hydrophone is connected to the fiber-optic hydrophone system (FOHSv2, Precision Acoustics) and the signal is read out with an oscilloscope (DSO-X 3032A, Agilent Technologies). The oscilloscope, function generator and 3-D-axis motorized stage can be controlled using a MATLAB-GUI on a computer. The hydrophone has a sensitivity of 268 mV/MPa at a frequency of 8 MHz. Linear interpolation gives a sensitivity of 281 mV/MPa for 8.4 MHz. The 3-D-printed holder for the measurements in the planar configuration can be seen in Fig. 7(a). A small custom-made PCB board is attached to connect the device to the oscilloscope connectors. The wire resistance of the connection between the oscilloscope connectors and the top metal layer of the PZT transducers was measured to be 2.3 Ω.

Before the acoustic measurements, a frequency sweep (from 1 to 16 MHz with a step of 0.1 MHz) was applied to the PZT-based US transducers to obtain the frequency of maximum acoustic pressure [see Fig. 7(d)]. For this measurement, a resonance frequency of 8.3 MHz was obtained, which is close to the expected value based on the mechanical resonance frequency of the PZT-5H material for a thickness of 267 μm. The acoustic profiles are measured in a zy plane parallel to the front of the device for different distances in the x-direction. The data is post-processed using a cubic interpolation method with 100 in between points at both axes. The scans for the 0.3- (near-field) and 1-mm (focal spot) distance can be found in Fig. 7(b) and (c), respectively. Each PZT-based US transducer has its own acoustic profile and some profile distortion is visible. The acoustic peak pressure varies among the PZT-based US transducers from 1.1 MPa to 700 kPa [see Fig. 7(c)], gaining 900 kPa on average. The focal spot of a single PZT-based US transducer has a size of around 100 $\times$ 200 μm. S_{tx} reaches 110 kPa/V.

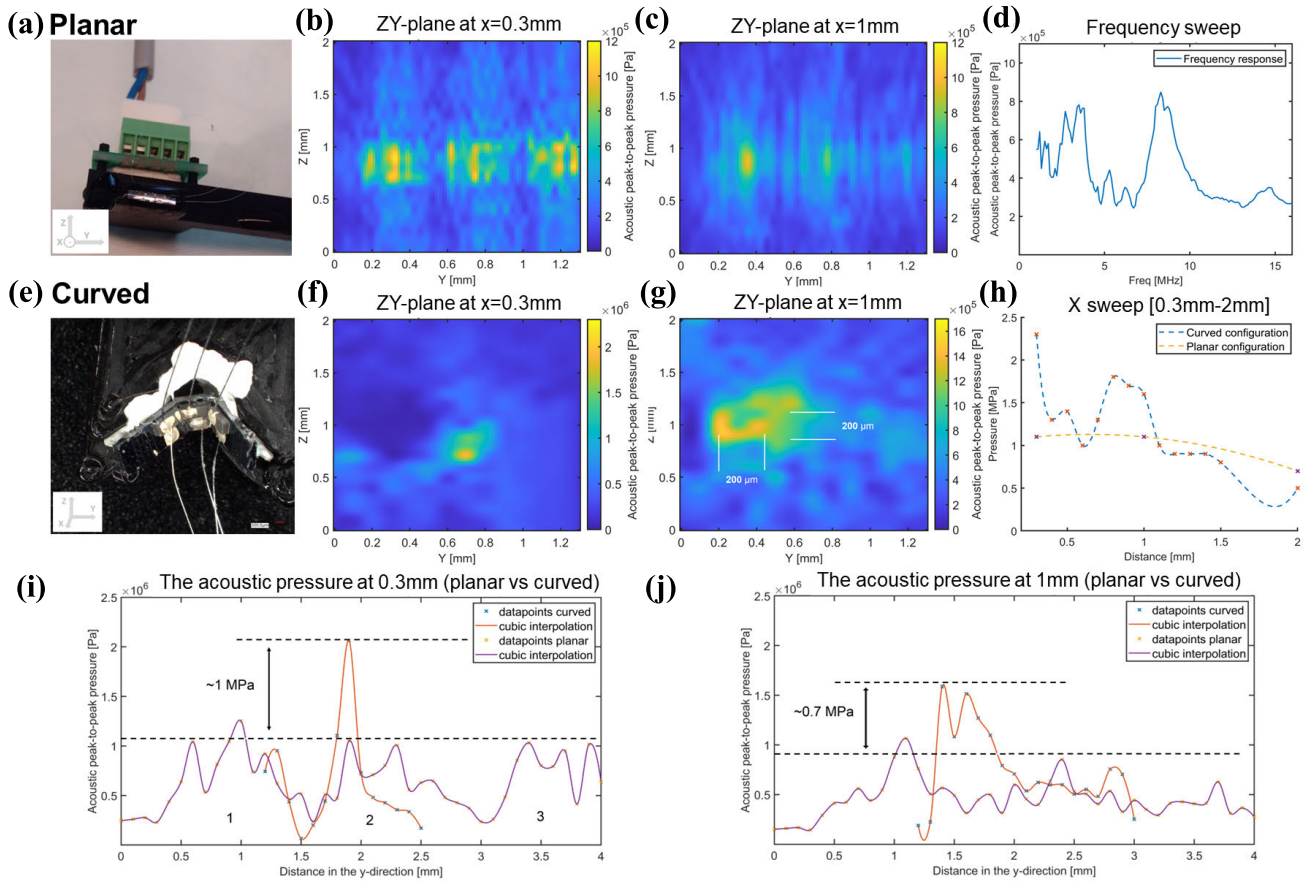

Fig. 7. Measurements (a) shows a photograph of the 3-D-printed holder with the device in a planar configuration, (b) and (c) show the acoustic profile for an *x*-distance parallel to the surface of the PZT-based US transducers of 0.3 and 1 mm, respectively, (d) shows the frequency response of one of the PZT-based US transducers from the planar configuration, (e) shows a micrograph of the design being curved in the 3-D-printed holder, (f) and (g) show the acoustic profile for an *x*-distance parallel to the surface of the middle PZT-based US transducer of 0.3 and 1 mm, respectively, (h) shows the pressure profiles of both the planar and curved configuration, (i) shows the pressure profiles along the white dashed lines in the acoustic profile of the curved and planar configuration at and *x*-distance of 0.3 mm, and (j) shows the pressure profiles along the white dashed lines in the acoustic profile of the curved and planar configuration at and *x*-distance of 1 mm.

A fully curved device can be observed in Fig. 8 with an inner radius of 0.95 mm. A top view of the setup of the curved sample in the water tank is given in Fig. 7(e). The 3-D-printed holder contains a half-circle, which, together with the device, has an inner diameter of 2 mm. The device is pushed inside the half-circle into a thin layer of glue pad that holds the device in a half-curved position. The acoustic profiles are scanned in the same way as for the planar configuration. The scans for 0.3 and 1 mm in the x-direction are shown in Fig. 7(f) and (g), respectively. The focal spot size is around 200 $\times$ 200 μm and is slightly larger than the simulations [see Fig. 7(g)].

The focal pressure magnitude in the curved configuration is increased by 0.7 MPa compared to the average focal pressure magnitude of the single PZT-based US transducer in the planar configuration [see Fig. 7(i) and (j)). Having a peak focal pressure of 1.6-MPa results in S_{tx} of 160 kPa/V. The pressure profiles of Fig. 7(i) and (j) are obtained from the cross sections of Fig. 7(b) and (c) at Z = 0.9 mm, from Fig. 7(f) at Z =0.7 mm, and from Fig. 7(g) at Z =1 mm. For the planar pressure profile line in Fig. 7(i), the locations of the PZT-based US transducers in the graph are indicated with the numbers 1, 2, and 3. In Fig. 7(h), the maximum focal pressures for each measurement in the curved and planar configuration are combined in a distance plot. The crosses indicate the maximum values, whereas the dashed line is an interpolation.

V. Discussion

The simulations show that the focal region of the cuff implant design has grating lobes resulting in high-intensity and high-pressure areas around the focal spot [see Fig. 2(f)]. This can potentially modulate unwanted regions in the VN. Beam steering could be implemented to reduce the impact of these grating lobes and target the nerve more specifically [36].

Comparing the results of the measurements with the simulations, it can be observed that the resonance frequency is well preserved after the fabrication of the device. The simulated resonance frequency is 8.4 MHz, whereas the measured resonance frequency is 8.3 MHz.

Moreover, from the comparison, it can be seen that the acoustic profile and the pressure levels differ. The distortion and harmonics at lower frequencies could be explained by the loading of the PZT-based US transducers due to the

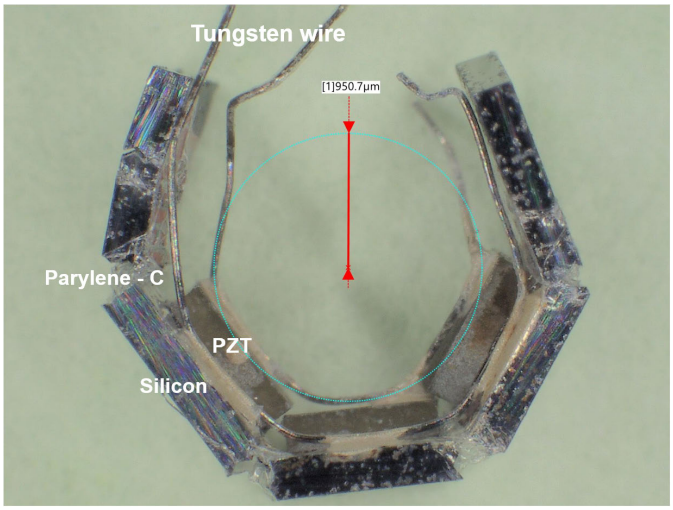

Fig. 8. Curvature of the island-bridge structure.

attachment of the tungsten wire changing the frequency behavior. Another reason might be the partial detachment of the PZT from the substrate as research shows that that can induce harmonics [66]. The detachment of the PZT from the substrate might be a consequence of poor adhesion to the ACF, placement variations of the PZTs, mechanical vibrations during operation or corrosion of the metal tracks due to water inlet via microcracks in the parylene-C encapsulation. This also has an impact on the output pressure levels. Moreover, the measurement in the curved configuration shows that a local maximum exists in the near-field that has a higher pressure magnitude than the focal spot [see Fig. 7(f)]. This could potentially result in unwanted VN areas being modulated. These near-field maxima are highly dependent on the medium and thus difficult to model [60]. They could, for instance, be reduced by implementing beam-steering [35], as this makes the focal spot less dependent on the exact PZT positioning, or improving the curvature of the device during the measurements. Moreover, as precise position control of the PZTs is crucial, the process parameters of the pick-and-place of the PZTs could be refined and automated, as this is a standard packaging step. This will result in even more precise (tolerance of up to 1 μm) PZT placement. Furthermore, in in vivo applications, the curved array has to follow the curvature of the VN, which is not expected to be perfectly cylindrical. In that case, reduction of the effects of transducer placement and substrate curvature on the beam profile can be highly mitigated by driving the transducers at different times and ensure constructive interference at the desired location. However, this might also lead to reduced focal pressure if any of the transducers are not directly facing the desired focal spot location, which can be compensated by increasing the driving voltage per individual transducer.

To reduce the profile and pressure variations and distortions even more, some other assembly steps could be fine-tuned. The pick-and-place process could be transformed into a top and backside dicing approach at which the dicing determines the alignment of the PZTs [35]. The manual attachment of the tungsten wire could be replaced by adding an evaporated or sputtered top metal plane on top of the PZT-based US transducers which will hypothetically reduce the distortion in the US profile.

Other reasons for the difference between the pressure profile in the simulations and the measured profile are the simplifications and idealities in the simulation model. In the simulation, only the PZT and a perfectly cylindrical parylene-C ring are taken into account. In reality, fabrication nonidealities, island-bridge instead of pure parylene-C, manual variations during PZT placement, and the attachment of the tungsten wire, degrade the performance of the PZT-based US transducer, leading to a different pressure profile. Moreover, the distortion of the focal spot might result from the nonperfect curvature and PZT placement variations. Due to small misalignments and tilting of the sample in the water tank during measurements in the planar configuration, there is a difference between the measured acoustic pressures among the PZT-based US transducers. Due to these differences, the absolute magnitude values have not been considered but the trends observed in the simulations. For both the simulations and the measurements, a proportional relation between the number of transducers and the acoustic output pressure or magnitude can be found. Moreover, a focal spot located around the center is simulated and measured.

The island-bridge structure with silicon islands and parylene-C interconnects gives flexibility and the ability of the device to have a curvature of 2 mm in diameter (see Fig. 8). However, as parylene-C is naturally brittle, it is still a vulnerability and the device should be handled with care. The robustness could be improved by increasing the layer thickness or creating a multilayer on top which protects the underlying parylene-C layer. However, this might affect the acoustic performance as the attenuation could increase, depending on the layer thickness, material properties, and the driving frequency. A biocompatible, transparent and cuff-implant-suitable alternative is polydimethylsiloxane (PDMS) [67]. Research shows that this material can be used in combination with parylene-C as an encapsulation layer [68], [69].

For the metal layer, AlSi (99%/1%) is used. However, during measurements, device failure occurs. This is likely due to the nonoptimized adhesion between the parylene-C and the metal tracks and the high water vapor transmission rate (WVTR) of parylene-C [70]. Posttreatment of the metal layer or replacing it by another more inert metal could improve the robustness of the metal layer [71]. Moreover, a multilayer encapsulation might increase the robustness [72] as well. Another advantage is that a multilayer encapsulation could be used for acoustic matching. A matching layer increases the acoustic power transfer between two nonmatching media (PZT and water) and will increase the acoustic output pressure [49]. The multilayer polymer-metal structure for acoustic matching might be promising as parylene-C can still be used as an encapsulation layer [73], [74], [75]. Besides, the backing layer can be optimized to minimize reflections by for example an air-backing layer [49]. Furthermore, electrical impedance matching could be considered to improve the power transfer performance [76].

To increase the acoustic output pressure even more, PZT-5H piezoelectric material could be replaced by the PMN-PT piezoelectric material as it has better electromechanical properties [77]. Moreover, beam steering could be implemented by dicing each individual PZT-based US transducer into a 2-D-phased array [35]. This opens the potential to target the VN at various locations within the radius of the cuff implant, thus expanding the range of stimulation with respect to the current design, which has a small, fixed focal spot. Another benefit of beam steering is the ability to compensate for mechanical deformation. In addition, in this research, opposing transducers were avoided due to the simulation results for this particular design. However, a full ring of US transducers could increase the acoustic output pressure which should be investigated in further research.

Although this article illustrates an early proof-of-concept, some crucial aspects of an implant have been considered. First of all, the designed size and dimensions are particularly meant for VNS at the level of the neck. Moreover, the materials have been selected to use wafer-level microfabrication to fabricate a bendable device, which may be expanded in the future to include different geometries and number of transducers. The processing steps have been ordered in such a way that the curvature of the device could be adapted after fabrication which is required in case of an implant. Nevertheless, bending the parylene material could lead to defects or detachment. A possible alternative to this approach would be to prebend the integrated device after transducer placement prior to parylene encapsulation. After this step, the required bending angle to match the curvature of the VN would be reduced from the native deposited parylene. A comprehensive biocompatibility study was not the main goal in this research. Biocompatibility concerns are, however, paramount for implantable devices, hence, this work aimed to set the foundations that will enable a biocompatible design. This was implemented by selecting the acoustic parameters and some of the materials. Damage of the tissue can occur when certain acoustic parameters are used (e.g., for tissue ablation). However, these have not been considered in this study, and thus the parameters for focused US without permanent tissue damage to the nerve [4] are taken into account in the proposed design. In addition, a medical grade parylene-C has been used in the microfabrication process. Furthermore, it should be noted that the embedded lead in the PZT transducers could potentially be harmful. Therefore, lead-free piezoelectric materials could be investigated, such as barium titanate and lithium niobate [49]. However, as the piezoelectric performance is slightly decreased and the material is more expensive, in this research PZT-5H transducers have been used.

The measurements show that the fabricated device in curved configuration has a high S_{tx}, indicating that per applied driving voltage to the device the output pressure increases with that amount (5)

$$P_{out} = V_{driving} * S_{tx}. \tag{5}$$

For a driving voltage of 10 V used in this study, the output pressure is $P_{out} = 160 * 10 = 1.6$ MPa using S_{tx} of 160 kPa/V. For comparison, CMUTs designed for VN neuromodulation have S_{tx} of 68 kPa/V [36]. In addition, a body-conformal active US patch presented by Pashaei et al. [25] shows S_{tx} of 80 kPa/V. This means that for similar driving voltages, significantly higher output pressures are obtained with this proposed design. The acoustic pressure output which has been measured at the focal spot in the curved configuration is 1.6 MPa. Literature is so far inconclusive regarding the required acoustic pressure output for neuromodulation of peripheral nerve targets [4], [6] but this may be within the range. In case higher acoustic pressure is required, research shows that there is a linear relation between the applied pressure and measured voltage of a piezoelectric material, including PZT [78]. As this effect is reversible, the relation between driving voltage and output acoustic pressure is also linear for a certain voltage range. In further research, a voltage sweep for the proposed design will be conducted, for which, a similar relationship is expected. As PZT transducers have a high voltage breakdown it is assumed that the required acoustic pressures for neuromodulation could be obtained. Due to fabrication inaccuracies linearity might not be obtained, affecting the efficiency, but therefore improvements for fabrication in future research will be implemented, such as replacing the tungsten wires by thin film patterning, and adding an acoustic air-backing layer. For future work, in vivo experiments are required to fully elucidate the effects of acoustic focusing at μm levels during VNS.

VI. Conclusion

This article proposes a 1 × 7 mm wafer-level microfabricated, island-bridge cuff implant with an inner diameter of 2 mm. COMSOL Multiphysics simulations have been performed to investigate the effect of the number of PZT-based US transducers and to verify the design. The wafer-level microfabrication and assembly consist of standardized and scalable process steps.

The device is driven at 8.3 MHz and has a focal length of 1 mm. Three commercial PZT-5H US transducers are integrated generating 0.9 MPa on average at the focal spot for each individual PZT-based US transducer in a planar configuration (S_{tx} = 110 kPa/V) whereas, 1.6 MPa is generated at the focal spot in curved configuration (S_{tx} = 160 kPa/V). The focal spot of the curved cuff implant is around 200 × 200 μm.

The measurements show the potential of a cuff-shape design with a PZT-based US transducer array as the output focal pressure is increased by at least 45% (taking the peak pressures at the focal spot for both the planar (1.1 MPa) and curved (1.6 MPa) configuration) compared to the measured focal pressures of the single PZT-based US transducers in the planar configuration. In conclusion, the integration of PZT-based US transducers in a cuff-shaped design is a first step which opens up a new path toward a novel technique for high-precision VNS.

Acknowledgment

The authors highly appreciated the support of the staff of the Else Kooi Lab at Delft University of Technology.

REFERENCES

[1] C. O. Oluigbo and A. R. Rezai, "Addressing neurological disorders with neuromodulation," *IEEE Trans. Biomed. Eng.*, vol. 58, no. 7, pp. 1907–1917, Jul. 2011.

[2] J. Blackmore, S. Shrivastava, J. Sallet, C. R. Butler, and R. O. Cleveland, "Ultrasound neuromodulation: A review of results, mechanisms and safety," *Ultrasound Med. Biol.*, vol. 45, no. 7, pp. 1509–1536, Jul. 2019.

[3] H. A. S. Kamimura, A. Conti, N. Toschi, and E. E. Konofagou, "Ultrasound neuromodulation: Mechanisms and the potential of multimodal stimulation for neuronal function assessment," *Frontiers Phys.*, vol. 8, p. 150, May 2020, doi: 10.3389/fphy.2020.00150.

[4] M. E. Downs, S. A. Lee, G. Yang, S. Kim, Q. Wang, and E. E. Konofagou, "Non-invasive peripheral nerve stimulation via focused ultrasound in vivo," *Phys. Med. Biol.*, vol. 63, no. 3, Jan. 2018, Art. no. 035011, doi: 10.1088/1361-6560/aa9fc2.

[5] M. G. Kim, H. A. S. Kamimura, S. A. Lee, C. Aurup, N. Kwon, and E. E. Konofagou, "Image-guided focused ultrasound modulates electrically evoked motor neuronal activity in the mouse peripheral nervous system in vivo," *J. Neural Eng.*, vol. 17, no. 2, Apr. 2020, Art. no. 026026.

[6] V. Cotero et al., "Peripheral focused ultrasound neuromodulation (pFUS)," *J. Neurosci. Methods*, vol. 341, Jul. 2020, Art. no. 108721.

[7] S. Kawasaki et al., "Pressure measurement of geometrically curved ultrasound transducer array for spatially specific stimulation of the vagus nerve," in *Proc. 9th Int. IEEE/EMBS Conf. Neural Eng. (NER)*, Mar. 2019, pp. 1239–1242, doi: 10.1109/NER.2019.8717064.

[8] H. Yuan and S. D. Silberstein, "Vagus nerve and vagus nerve stimulation, a comprehensive review: Part I," *Headache, J. Head Face Pain*, vol. 56, no. 1, pp. 71–78, Jan. 2016.

[9] M. Settell et al., "Functional vagotopy in the cervical vagus nerve of the domestic pig: Implications for the study of vagus nerve stimulation," *J. Neural Eng.*, vol. 17, no. 2, 2020.

[10] N. Jayaprakash et al., "Organ- and function-specific anatomical organization of vagal fibers supports fascicular vagus nerve stimulation," *Brain Stimulation*, vol. 16, no. 2, pp. 484–506, Mar. 2023.

[11] D. A. Groves and V. J. Brown, "Vagal nerve stimulation: A review of its applications and potential mechanisms that mediate its clinical effects," *Neurosci. Biobehavioral Rev.*, vol. 29, no. 3, pp. 493–500, May 2005.

[12] R. L. Johnson and C. G. Wilson, "A review of vagus nerve stimulation as a therapeutic intervention," *J. Inflammation Res.*, vol. 11, pp. 203–213, May 2018.

[13] M. Panebianco, A. Rigby, and A. G. Marson, "Vagus nerve stimulation for focal seizures," *Cochrane Database Systematic Rev.*, vol. 2022, pp. 1–43, 2022, doi: 10.1002/14651858.CD002896.

[14] R. Howland, "Vagus nerve stimulation," *Current Behav. Neurosci. Rep.*, vol. 1, pp. 64–73, Jun. 2014.

[15] S. Lee, W. Y. X. Peh, N. V. Thakor, S. C. Yen, and C. Lee, "Vagus nerve stimulation (VNS) for heart rate control using novel neural interfaces," in *Proc. 19th Int. Conf. Solid-State Sensors, Actuators Microsystems*, 2017, pp. 1730–1733.

[16] H. Yuan and S. D. Silberstein, "Vagus nerve and vagus nerve stimulation, a comprehensive review: Part II," *Headache, J. Head Face Pain*, vol. 56, no. 2, pp. 259–266, Feb. 2016.

[17] T. V. H. F. Oliveira, A. N. Francisco, Z. Demartini, and S. L. Stebel, "The role of vagus nerve stimulation in refractory epilepsy," *Arquivos de Neuro-Psiquiatria*, vol. 75, no. 9, pp. 657–666, 2017.

[18] E. W. Dirr, Y. A. Patel, L. Lester, F. Delgado, and K. J. Otto, "Targeted vagus nerve stimulation does not disrupt cardiac function in the diabetic rat," in *Proc. 41st Annu. Int. Conf. IEEE Eng. Med. Biol. Soc.*, Jul. 2019, pp. 6286–6289.

[19] V. Giagka and W. A. Serdijn, "Realizing flexible bioelectronic medicines for accessing the peripheral nerves—Technology considerations," *Bioelectronic Med.*, vol. 4, no. 1, p. 8, Dec. 2018, doi: 10.1186/s42234-018-0010-y.

[20] J. Y. Y. Yap, C. Keatch, E. Lambert, W. Woods, P. R. Stoddart, and T. Kameneva, "Critical review of transcutaneous vagus nerve stimulation: Challenges for translation to clinical practice," *Frontiers Neurosci.*, vol. 14, p. 284, Apr. 2020.

[21] S. De Smet et al., "Non-invasive vagal nerve stimulation enhances cognitive emotion regulation," *Behaviour Res. Therapy*, vol. 145, Oct. 2021, Art. no. 103933.

[22] K. Shin, Y. M. Bae, H. S. Park, D. G. Kang, and M. Kang, "The effect of electrode distance on the voltage distribution during non-invasive vagus nerve stimulation—A preliminary study," in *Proc. Int. Conf. Electron., Inf., Commun.*, 2023, pp. 1–3.

[23] A. Levitsky, J. Klein, P. K. Artemiadis, and C. A. Buneo, "Effects of transcutaneous electric nerve stimulation on upper extremity proprioceptive function," in *Proc. 42nd Annu. Int. Conf. IEEE Eng. Med. Biol. Soc. (EMBC)*, Jul. 2020, pp. 3577–3580.

[24] N. Gurel et al., "Toward closed-loop transcutaneous vagus nerve stimulation using peripheral cardiovascular physiological biomarkers: A proof-of-concept study," in *Proc. IEEE 15th Int. Conf. Wearable Implant. Body Sensor Netw. (BSN)* Jul. 2018, pp. 78–81.

[25] V. Pashaei, P. Dehghanzadeh, G. Enwia, M. Bayat, S. J. A. Majerus, and S. Mandal, "Flexible body-conformal ultrasound patches for image-guided neuromodulation," *IEEE Trans. Biomed. Circuits Syst.*, vol. 14, no. 2, pp. 305–318, Apr. 2020.

[26] E. H. Rijnbeek, N. Eleveld, and W. Olthuis, "Update on peripheral nerve electrodes for closed-loop neuroprosthetics," *Frontiers Neurosci.*, vol. 12, May 2018, Art. no. 314838.

[27] F. J. Rodri et al., "Polyimide cuff electrodes for peripheral nerve stimulation," *J. Neurosci. Methods*, vol. 98, no. 2, pp. 105–118, Jun. 2000.

[28] T. Stieglitz, H. Beutel, M. Schuettler, and J. U. Meyer, "Micromachined, polyimide-based devices for flexible neural interfaces," *Biomed. Microdevices*, vol. 2, pp. 283–294, Dec. 2000.

[29] M. Forssell et al., "Compliant adhesive cuff electrode for selective stimulation in rat vagus nerve," in *Proc. IEEE SENSORS*, Oct. 2019, pp. 1–4.

[30] M. Haugland, "A flexible method for fabrication of nerve cuff electrodes," in *Proc. 18th Annu. Int. Conf. IEEE Eng. Med. Biol. Soc.*, Mar. 1997, pp. 359–360.

[31] M. J. Freeberg, M. A. Stone, R. J. Triolo, and D. J. Tyler, "The design of and chronic tissue response to a composite nerve electrode with patterned stiffness," *J. Neural Eng.*, vol. 14, no. 3, Jun. 2017, Art. no. 036022, doi: 10.1088/1741-2552/aa6632.

[32] D. Tyler and D. Durand, "A slowly penetrating interfascicular nerve electrode for selective activation of peripheral nerves," *IEEE Trans. Rehabil. Eng.*, vol. 5, no. 1, pp. 51–61, Mar. 1997.

[33] G. Kim et al., "Recent progress on microelectrodes in neural interfaces," *Materials*, vol. 11, no. 10, p. 1995, Oct. 2018, doi: 10.3390/ma11101995.

[34] K. A. Yildiz, A. Y. Shin, and K. R. Kaufman, "Interfaces with the peripheral nervous system for the control of a neuroprosthetic limb: A review," *J. NeuroEngineering Rehabil.*, vol. 17, no. 1, pp. 1–19, Dec. 2020.

[35] T. Costa, C. Shi, K. Tien, J. Elloian, F. A. Cardoso, and K. L. Shepard, "An integrated 2D ultrasound phased array transmitter in CMOS with pixel pitch-matched beamforming," *IEEE Trans. Biomed. Circuits Syst.*, vol. 15, no. 4, pp. 731–742, Aug. 2021.

[36] S. Kawasaki, E. Dijkema, M. Saccher, V. Giagka, J. Schleipen, and R. Dekker, "Schlieren visualization of focused ultrasound beam steering for spatially specific stimulation of the vagus nerve," in *Proc. 10th Int. IEEE EMBS Conf. Neural Eng. (NER)*, May 2021, pp. 1113–1116, doi: 10.1109/NER49283.2021.9441225.

[37] W. O'Brien, "Ultrasound-biophysics mechanisms," *Prog. Biophys. Mol. Biol.*, vol. 93, pp. 212–255, Jan. 2007.

[38] H. Kele, "Ultrasonography of the peripheral nervous system," *Perspect. Med.*, vol. 1, nos. 1–12, pp. 417–421, Sep. 2012.

[39] E. J. Juan, R. González, G. Albors, M. P. Ward, and P. Irazoqui, "Vagus nerve modulation using focused pulsed ultrasound: Potential applications and preliminary observations in a rat," *Int. J. Imag. Syst. Technol.*, vol. 24, no. 1, pp. 67–71, Mar. 2014, doi: 10.1002/ima.22080.

[40] V. Colucci, G. Strichartz, F. Jolesz, N. Vykhodtseva, and K. Hynynen, "Focused ultrasound effects on nerve action potential in vitro," *Ultrasound Med. Biol.*, vol. 35, pp. 1737–1747, Oct. 2009.

[41] J. L. Foley, J. W. Little, and S. Vaezy, "Effects of high-intensity focused ultrasound on nerve conduction," *Muscle Nerve*, vol. 37, no. 2, pp. 241–250, Feb. 2008.

[42] M. Plaksin, S. Shoham, and E. Kimmel, "Intramembrane cavitation as a predictive bio-piezoelectric mechanism for ultrasonic brain stimulation," *Phys. Rev. X*, vol. 4, no. 1, Jan. 2014, Art. no. 011004.

[43] T. Heimburg and A. D. Jackson, "On soliton propagation in biomembranes and nerves," *Proc. Nat. Acad. Sci. USA*, vol. 102, no. 28, pp. 9790–9795, Jul. 2005, doi: 10.1073/pnas.0503823102.

[44] S. Oh et al., "Ultrasonic neuromodulation via astrocytic TRPA1," *Current Biol.*, vol. 29, pp. 3386–3401, Oct. 2019.

[45] S. H. Lee, J. H. Jung, Y. M. Chae, and J. Y. Kang, "Fabrication and characteristics of the implantable and flexible nerve cuff electrode for neural interfaces," in *Proc. 4th Int. IEEE/EMBS Conf. Neural Eng.*, Apr. 2009, pp. 80–83.

[46] N. Ji et al., "Autonomic modulation by low-intensity focused ultrasound stimulation of the vagus nerve," *J. Neural Eng.*, vol. 19, no. 6, Dec. 2022, Art. no. 066036.

[47] K. M. Wasilczuk et al., "Modulating the inflammatory reflex in rats using low-intensity focused ultrasound stimulation of the vagus nerve," *Ultrasound Med. Biol.*, vol. 45, no. 2, pp. 481–489, Feb. 2019.

[48] Y. Imamura et al., "Ultrasound stimulation of the vagal nerve improves acute septic encephalopathy in mice," *Frontiers Neurosci.*, vol. 17, Jul. 2023, Art. no. 1211608.

[49] V. T. Rathod, "A review of acoustic impedance matching techniques for piezoelectric sensors and transducers," *Sensors*, vol. 20, no. 14, p. 4051, Jul. 2020.

[50] K. Shen and M. M. Maharbiz, "Design of ceramic packages for ultrasonically coupled implantable medical devices," *IEEE Trans. Biomed. Eng.*, vol. 67, no. 8, pp. 2230–2240, Aug. 2020.

[51] Z. Wang et al., "A flexible ultrasound transducer array with micro-machined bulk PZT," *Sensors*, vol. 15, no. 2, pp. 2538–2547, Jan. 2015.

[52] Y. Yang et al., "A flexible piezoelectric micromachined ultrasound transducer," *RSC Adv.*, vol. 3, no. 47, p. 24900, 2013.

[53] I. Wygant, "A comparison of CMUTs and piezoelectric transducer elements for 2D medical imaging based on conventional simulation models," in *Proc. IEEE Int. Ultrason. Symp.*, Oct. 2011, pp. 100–103.

[54] E. Ledesma et al., "Squared PMUT with enhanced pressure sensitivities," in *Proc. MDPI*, 2018, p. 925.

[55] F. Akasheh, T. Myers, J. D. Fraser, S. Bose, and A. Bandyopadhyay, "Development of piezoelectric micromachined ultrasonic transducers," *Sens. Actuators A, Phys.*, vol. 111, pp. 275–287 Mar. 2004.

[56] B. Lee, A. Nikoozadeh, K. Park, and B. Khuri-Yakub, "High-efficiency output pressure performance using capacitive micromachined ultrasonic transducers with substrate-embedded springs," *Sensors*, vol. 18, no. 8, p. 2520, Aug. 2018.

[57] POSITION Consortium. (2021). *A European MEMS Ultrasound Benchmark*. Accessed Dec. 22, 2023. [Online]. Available: http://position-2.eu/whitepapers/

[58] H. Rivandi and T. L. Costa, "A 2D ultrasound phased-array transmitter ASIC for high-frequency ultrasound stimulation and powering," *IEEE Trans. Biomed. Circuits Syst.*, vol. 17, no. 4, pp. 701–712, Aug. 2023.

[59] *Comsol Acoustics Module User's Guide*. Accessed: Aug. 21, 2023. [Online]. Available: https://doc.comsol.com/5.4/doc/com.comsol.help.aco/AcousticsModu leUsersGuide.pdf

[60] H. S. Gougheri, A. Dangi, S.-R. Kothapalli, and M. Kiani, "A comprehensive study of ultrasound transducer characteristics in microscopic ultrasound neuromodulation," *IEEE Trans. Biomed. Circuits Syst.*, vol. 13, no. 5, pp. 835–847, Oct. 2019.

[61] C. Shi, T. Costa, J. Elloian, and K. L. Shepard, "Monolithic integration of micron-scale piezoelectric materials with CMOS for biomedical applications," in *IEDM Tech. Dig.*, 2018, pp. 1–4.

[62] C. Shi et al., "Application of a sub–0.1-mm^3 implantable mote for in vivo real-time wireless temperature sensing," *Sci. Adv.*, vol. 7, no. 19, May 2021, Art. no. eabf6312, doi: 10.1126/sciadv.abf6312.

[63] C. Shi, T. Costa, J. Elloian, Y. Zhang, and K. L. Shepard, "A 0.065-mm^3 monolithically-integrated ultrasonic wireless sensing mote for real-time physiological temperature monitoring," *IEEE Trans. Biomed. Circuits Syst.*, vol. 14, no. 3, pp. 412–424, Jun. 2020.

[64] J. Ortigoza-Diaz et al., "Techniques and considerations in the microfabrication of parylene C microelectromechanical systems," *Micromachines*, vol. 9, no. 9, p. 422, Aug. 2018, doi: 10.3390/mi9090422.

[65] M. K. Khaw, F. Mohd-Yasin, and N. T. Nguyen, "Microcalorimeter: Design considerations, materials and examples," *Microelectronic Eng.*, vol. 158, pp. 107–117, Jul. 2016.

[66] N. P. Yelve, M. Mitra, and P. M. Mujumdar, "Higher harmonics induced in Lamb wave due to partial debonding of piezoelectric wafer transducers," *NDT E Int.*, vol. 63, pp. 21–27, Apr. 2014.

[67] I. Miranda et al., "Properties and applications of PDMS for biomedical engineering: A review," *J. Funct. Biomaterials*, vol. 13, no. 1, p. 2, Dec. 2021.

[68] N. B. Babaroud, R. Dekker, W. Serdijn, and V. Giagka, "PDMS-parylene adhesion improvement via ceramic interlayers to strengthen the encapsulation of active neural implants," in *Proc. 42nd Annu. Int. Conf. IEEE Eng. Med. Biol. Soc. (EMBC)*, Jul. 2020, pp. 3399–3402, doi: 10.1109/EMBC44109.2020.9175646.

[69] N. B. Babaroud et al., "Investigation of the long-term adhesion and barrier properties of a PDMS-parylene stack with PECVD ceramic interlayers for the conformal encapsulation of neural implants," in *Proc. 23rd Eur. Microelectron. Packag. Conf. Exhib. (EMPC)*, Sep. 2021, pp. 1–7, doi: 10.23919/EMPC53418.2021.9584961.

[70] K. Nanbakhsh et al., "Effect of signals on the encapsulation performance of parylene coated platinum tracks for active medical implants," in *Proc. 41st Annu. Int. Conf. IEEE Eng. Med. Biol. Soc. (EMBC)*, Jul. 2019, pp. 3840–3844, doi: 10.1109/EMBC.2019.8857702.

[71] M. A. Mahmood, D. Chioibasu, A. U. Rehman, S. Mihai, and A. Popescu, "Post-processing techniques to enhance the quality of metallic parts produced by additive manufacturing," *Metals*, vol. 12, no. 1, p. 7, 2022.

[72] A. Pak et al., "Thin film encapsulation for LCP-based flexible bioelectronic implants: Comparison of different coating materials using test methodologies for life-time estimation," *Micromachines*, vol. 13, no. 4, p. 544, Mar. 2022, doi: 10.3390/mi13040544.

[73] C. Fei et al., "Design of matching layers for high-frequency ultrasonic transducers," *Appl. Phys. Lett.*, vol. 107, no. 12, Sep. 2015, Art. no. 123505, doi: 10.1063/1.4931703.

[74] M. Toda and M. Thompson, "Detailed investigations of polymer/metal multilayer matching layer and backing absorber structures for wideband ultrasonic transducers," *IEEE Trans. Ultrason., Ferroelectr., Freq. Control*, vol. 59, no. 2, pp. 231–242, Feb. 2012.

[75] X. Yang et al., "Multi-layer polymer-metal structures for acoustic impedance matching in high-frequency broadband ultrasonic transducer design," *Appl. Acoust.*, vol. 160, Mar. 2019, Art. no. 107123.

[76] V. T. Rathod, "A review of electric impedance matching techniques for piezoelectric sensors, actuators and transducers," *Electronics*, vol. 8, no. 2, p. 169, Feb. 2019.

[77] K.-B. Kim, D. K. Hsu, B. Ahn, Y.-G. Kim, and D. J. Barnard, "Fabrication and comparison of PMN-PT single crystal, PZT and PZT-based 1–3 composite ultrasonic transducers for NDE applications," *Ultrasonics*, vol. 50, no. 8, pp. 790–797, Aug. 2010.

[78] M. M. S. Dezfouli, M. R. Hassan, M. H. Ruslan, S. Mat, and B. Bakhtyar, "Experimental and theoretical investigations of the impact localization of a passive smart composite plate fabricated using piezoelectric materials," *Adv. Mater. Sci. Eng.*, vol. 2013, pp. 1–12, Jan. 2013.

Cornelis van Damme was born in Goes, The Netherlands, in 2000. He received the B.Sc. degree in electrical engineering including a robotics minor from Delft University of Technology, Delft, The Netherlands, in 2021, and the M.Sc. degree in microelectronics from Delft University of Technology, with bioelectronics as his specialization focusing on microfabrication in 2023. His thesis work was related to integrating ultrasound transducers in a miniaturized cuff for vagus nerve neuromodulation.

Since 2022, he has been participating in a biosystems engineering master's program at Wageningen University, Wageningen, The Netherlands. His research and thesis work is related to sensors and robotics. Since 2023, he has been participating in a reformed theology master's program at Apeldoorn Theological University, Apeldoorn, The Netherlands, which is related to theology, ethics, and technology.

Gandhika K. Wardhana (Graduate Student Member, IEEE) received the B.Sc. degree in electrical engineering from Bandung Institute of Technology, Bandung, Indonesia, in 2015, and the M.Sc. degree in electrical engineering focusing on microelectronics from Delft University of Technology, Delft, The Netherlands, in 2019, where he is currently pursuing the Ph.D. degree under the direction of Tiago L. Costa and Massimo Mastrangeli in developing a brain-on-a-chip platform to study ultrasound neuromodulation.

His research interests include the fabrication of ultrasound microsystems and MEMS for biomedical applications.

Andrada Iulia Velea (Graduate Student Member, IEEE) was born in Timişoara, Romania, in 1994. She received the B.Sc. degree in electronics and telecommunications from the Polytechnic University of Timisoara, Timişoara, in 2017, and the M.Sc. degree (cum laude) in biomedical engineering from the Technical University of Delft, Delft, The Netherlands, in 2019, where she is currently pursuing the Ph.D. degree, focusing on the investigation and development of active neural interfaces using ultrasound and electricity as a means of neuromodulation.

From 2020 to 2023, she was involved in the European project, Moore4Medical (M4M), which aimed to accelerate innovation in emerging medical application through open technology platforms. Since 2020, she has also been a part of the Technologies for Bioelectronics Group, Fraunhofer Institute for Reliability and Microintegration (IZM), Berlin, Germany.

Vasiliki (Vasso) Giagka (Senior Member, IEEE) was born in Athens, Greece, in 1984. She received the M.Eng. degree in electronic and computer engineering from the Aristotle University of Thessaloniki, Thessaloniki, Greece, in 2009, and the Ph.D. degree in electronic engineering from University College London, London, U.K., in 2014.

She spent six months as a Postdoctoral Researcher at the Implanted Devices Group, University College London. Since September 2015, she has been an Assistant Professor at Delft University of Technology, Delft, The Netherlands. Since September 2018, she has also been leading the Technologies for Bioelectronics Group, Fraunhofer Institute for Reliability and Microintegration IZM, Berlin, Germany. Between her two affiliations, she is carrying out research on the design and fabrication of active neural interfaces. In particular, she is investigating new approaches for neural stimulation and wireless power transfer, as well as implant miniaturization, microsystem integration, packaging, and encapsulation to meet the challenges of bioelectronic medicines.

Tiago L. Costa (Senior Member, IEEE) received the B.Sc. and M.Sc. degrees in electrical engineering and the Ph.D. degree in electrical and computer engineering from the Instituto Superior Técnico (IST), University of Lisbon, Lisbon, Portugal, in 2006, 2008, and 2014, respectively. His Ph.D. thesis focused on the development of CMOS integrated circuits for magnetoresistive sensors interface for biomolecular recognition and neuronal recording.

From 2015 to the summer of 2019, he was a Postdoctoral Research Associate at the Bioelectronics Systems Laboratory, Columbia University, New York, NY, USA, where he worked on ultrasound phased array systems for noninvasive nerve stimulation and wireless power transfer and data telemetry. Since October 2019, he has been an Assistant Professor of bioelectronics at Delft University of Technology, Delft, The Netherlands, where his group is pursuing the development of ultrasound microsystems for the next-generation neurotechnologies.